Dynamic Heterogeneity and Stretched Exponential Distributions in Cargo Transport within Living Cells

Yusheng Shen,[1] Yan Wen,[1] Qirui Zhao,[2] Pingbo Huang,[2] Pik-Yin Lai,[3,4,*] and Penger Tong[1,†]
[1]Department of Physics, Hong Kong University of Science and Technology, Clear Water Bay, Kowloon, Hong Kong
[2]Division of Life Science and State Key Laboratory of Molecular Neuroscience, Hong Kong University of Science and Technology, Clear Water Bay, Kowloon, Hong Kong
[3]Department of Physics and Center for Complex Systems, National Central University, Taoyuan City 320, Taiwan
[4]Physics Division, National Center for Theoretical Sciences, Taipei 10617, Taiwan

(Received 25 August 2025; accepted 6 July 2026; published 4 August 2026)

Stretched exponential distributions of nonequilibrium steady-state fluctuations are ubiquitous in living and nonliving systems alike, yet their microscopic origins have remained elusive. In this Letter, we track the motion of three types of vesicles across different cell types and find that their trajectories undergo random transitions between directed runs (on state) and diffusionlike jiggling (off state) in the highly dynamic, heterogeneous cytoplasm. The dwell times in these two states follow a stretched exponential distribution, which arises from a continuous weighted sum of simple exponential distributions that align with the unbinding kinetics of motor proteins traversing the cytoskeletal filaments *in vitro*. Our findings illuminate the profound connection between stretched exponential statistics and dynamic heterogeneity, shedding new light on the complex spatiotemporal landscape of cargo transport within cells.

DOI: 10.1103/ngxy-z1d3

How proteins navigate and function in densely packed cells is an outstanding issue in cell biology, which has been the subject of ongoing debate [1–6]. There exist two physical modes of intracellular transport [7]: passive diffusion of biomolecules at short distances (nm − μm scale) and active, motor-driven transport of vesicular cargoes over long distances (μm to the cell's size). For normal diffusion at equilibrium, the central limit theorem guarantees that the probability density function (PDF) $\mathcal{P}(\Delta x)$ of particle displacement $\Delta x(t)$ follows the Gaussian distribution, and deviations (when present) decay with lag time t. Thermal motion in crowded or heterogeneous environments, such as protein diffusion in cells [8–12], commonly produces non-Gaussian (typically exponential) displacement distributions even when the mean-squared displacement remains linear in time [13–15].

Various models have been proposed to explain the non-Gaussian behavior in terms of heterogeneity, broad diffusivity distributions, trapping, or Lévy-type jumps [16–19]. Among them, a compelling hypothesis suggests that the non-Gaussian PDF $\mathcal{P}(\Delta x)$ may arise from dynamic heterogeneity in cells, such as from a protein's diffusivity D. In this case, the PDF $\mathcal{P}(\Delta x)$ can be written as a superposition of the "fundamental modes" (or conditional PDF) $G(\Delta x|D)$ [11,20–22],

$$\mathcal{P}(\Delta x) = \int_0^\infty G(\Delta x|D)p(D)dD, \tag{1}$$

where $G(\Delta x|D)$ is a Gaussian for protein diffusion at a given value of D, and $p(D)$ is a distribution function of D. When D has a broad distribution, such as an exponential distribution, $p(D) \propto \exp(-D/D_0)$, the resulting $\mathcal{P}(\Delta x)$ exhibits a long exponential tail [11,20–22], which falls off much slower than a Gaussian. Recent experimental studies on protein diffusion on live cell membranes have confirmed this mechanism [11,12].

In contrast, motor-driven cargo transport is characterized by persistent directed motion interrupted by intermittent "pauses," during which the vesicles exhibit jiggling motion [23–28]. Because multiple molecular motors introduce persistent temporal correlations while cooperatively pulling the vesicle, the dwell times in both the active ("on") state and the pausing ("off") state become key observables for characterizing nonequilibrium cargo transport. These dwell times are positive random variables. They would follow Poisson statistics with a simple exponential distribution, if the underlying switching kinetics were purely random, homogeneous, and statistically independent (without correlations). Deviations from this exponential behavior, therefore, signal the presence of nontrivial collective dynamics and new underlying physics.

Here, we show that the dwell time statistics for the vesicles in both the on and off states follow a stretched exponential distribution, $\mathcal{P}(\tau) \propto \exp(-\tau/\tau_0)^\beta$, where τ is a dwell time with τ_0 being its characteristic value and the

*Contact author: pylai@phy.ncu.edu.tw
†Contact author: penger@ust.hk

exponent $0 < \beta < 1$. The stretched exponential distribution is non-Gaussian but for mechanistically different reasons, as will be shown below. It has been widely used to characterize relaxations in disordered systems and nonequilibrium fluctuations in steady states [29,30]. Thus far, the stretched exponential distribution is mainly used as a phenomenological description, and understanding its physical origin remains a challenge. Previous efforts to explain stretched exponential relaxation as a continuous weighted sum of simple exponential decays originating from Debye relaxations [31–34] have yet to be experimentally validated. The applicability of this argument to nonequilibrium steady states is still an open question.

In this Letter, we employ advanced single-particle tracking and sorting algorithms to capture the moving trajectory of various vesicles driven by motor proteins, such as dynein and kinesin, along with cytoskeletal filaments inside a cell at a spatial resolution of ~20 nm [12,35]. The vesicles under investigation include late-stage endocytic vesicles containing epidermal growth factor receptors (EGFR endosomes), early endosomes (EEs), and lysosomes. These vesicles cover a wide range of organelles, which are transported by distinct sets of microtubule motors and regulators [36,37]. The cell types examined cover both normal and cancerous epithelial cells from various tissue origins, including the human bronchial epithelial cell line (BEAS-2B), the human cervical cancer cell line (HeLa), and human retinal pigment epithelial-1 cells (RPE-1). By analyzing the recorded vesicle positions $\mathbf{r}(t)$ over time t, we collect an extensive dataset of vesicle trajectories from over 485 cells, covering a wide range of sampling times and traveling distances across the entire cell (see Sec. I in Supplemental Material for more details [38]).

Figure 1(a) shows a collection of 3-min-long mobile trajectories of EGFR endosomes in RPE-1 cells. The trajectories of individual vesicles all exhibit irregular motion patterns, including intermittent runs ("on state"), pauses ("off state"), and reversals, as illustrated in Figs. 1(b) and 1(c). The on state is characterized by directed motion along relatively straight and extended paths, while the off state involves jiggling or diffusionlike movement with minimal displacement. Although such a two-state motion has been previously reported for specific endosomes, lysosomes, and secretory vesicles at certain intracellular positions [23–28], our Letter reveals that the two-state transport is a common feature for various motor-driven vesicles across different cell types and over a wide range of travel distances across the entire cell.

To analyze the statistical properties of the on-state and off-state trajectory segments separately, we employ an automated selection algorithm developed by Röding *et al.* [50] to distinguish between the two states in each trajectory (see Supplemental Material, Sec. I for details [38]). Once the segments are identified, we label each vesicle trajectory with its on-state probability p_{on}, defined by the fractional time spent in the on state. The entire set of vesicle trajectories can then be categorized into two groups: the immobile group with $p_{\mathrm{on}} = 0$ and the mobile group with $p_{\mathrm{on}} > 0$.

Figure 1(c) displays 11 representative mobile lysosome trajectories with different values of p_{on}. The vesicles demonstrate considerable dynamic heterogeneity, as evidenced by significant variation in trajectory shapes and sizes; some are mobile [illustrated by the colored trajectories in Fig. 1(a)], while others are nearly immobile (not shown here). Among the mobile vesicles, some exhibit rapid movement (long trajectories), while others move

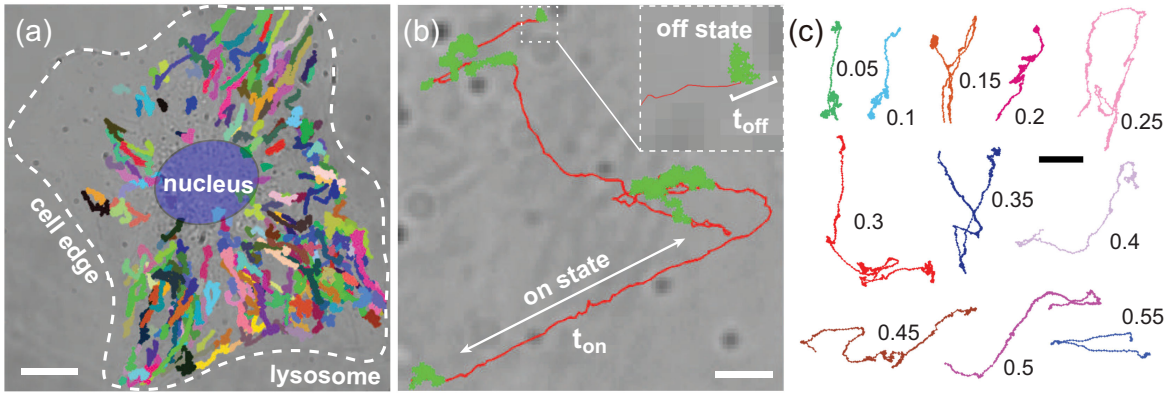

FIG. 1. Cargo transport in a living cell. (a) A total of 258 representative mobile trajectories (colored lines) superimposed on a simultaneously taken bright-field image of a BEAS-2B cell, showing the intracellular motion of lysosomes. The trajectories are computed over 1800 time steps (180 s long). The white dashed line indicates the cell periphery, and the blue ellipse indicates the cell nucleus. The scale bar is 10 μm. (b) A representative mobile trajectory of a lysosome showing intermittent switching between the on state (red) and off state (green). The inset provides a magnified view of a section of the trajectory. The scale bar is 2 μm. (c) A total of 11 representative mobile trajectories of lysosomes with varying on-state probabilities p_{on}, as marked by a nearby number. The scale bar is 5 μm.

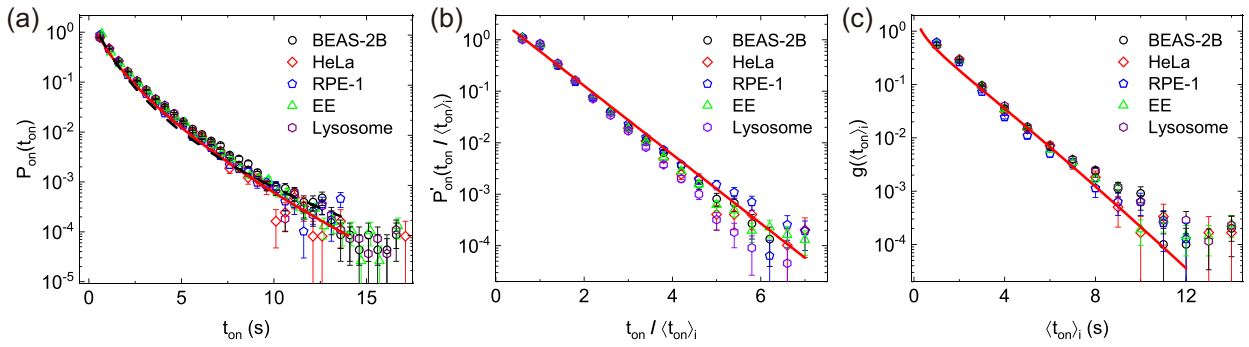

FIG. 2. Statistics of on-state dwell time t_{on}. (a) Measured PDFs $P_{on}(t_{on})$ for EGFR endosomes in BEAS-2B cells (black circles), HeLa cells (red diamonds), and RPE-1 cells (blue pentagons), and for early endosomes (EE, green triangles) and lysosomes (purple hexagons) in BEAS-2B cells. The red solid line shows a representative fit of Eq. (2) to the EGFR-endosome data from RPE-1 cells with $\tau_0 = 0.29 \pm 0.10$ s and $\beta = 0.61 \pm 0.04$. Fits to other datasets are shown in Fig. 4 (End Matter). The black dashed line shows the calculated $P_{on}(t_{on})$ using Eq. (4) and the measured $g(\langle t_{on}\rangle_i)$ in (c) for EGFR-endosomes in RPE-1 cells. (b) Measured PDFs $P'_{on}(t_{on}/\langle t_{on}\rangle_i)$ of the normalized dwell time $t_{on}/\langle t_{on}\rangle_i$. The red solid line shows a fit of Eq. (3) to the RPE-1 data with $a = 1.55 \pm 0.05$. Fits to other datasets are shown in Fig. 5 (End Matter). (c) Measured distribution functions $g(\langle t_{on}\rangle_i)$ of the trajectory-based mean dwell time $\langle t_{on}\rangle_i$ for different vesicles across various cell types. The red solid line shows a fit of Eq. (S6) in Supplemental Material with $\tau_0 = 0.52 \pm 0.10$ s and $\beta = 0.54 \pm 0.04$ for EGFR endosomes in RPE-1 cells (see Supplemental Material, Sec. III.C for more details [38]).

more slowly (shorter trajectories). The values of p_{on} for these trajectories range widely from 0 to 1. For EGFR endosomes in RPE-1 cells, we observe that the immobile group comprises approximately half of the trajectories ($49 \pm 13\%$, averaging across 42 cells) and is predominantly trapped in the perinuclear region. In contrast, the mobile group generally exhibits a radial pattern around the cell nucleus [see Fig. 1(a)], closely resembling the microtubule arrangement in a cell. These mobile trajectories are highly heterogeneous, with faster-moving vesicles (and large values of p_{on}) primarily localized near the cell's periphery.

From the extensive collection of extracted on-state and off-state segments, we compute the statistics of the on-state dwell time t_{on} and off-state dwell time t_{off} for various vesicles across different cell types. Typically, we find 3–15 moving segments in each trajectory, from which we compute t_{on} for each segment and the mean value $\langle t_{on}\rangle_i$ for that (the i th) trajectory. The probability density functions (PDFs) $P_{on}(t_{on})$, as shown in Fig. 2(a), are averaged over an ensemble of trajectories from multiple cells of the same type cultured under the same experimental conditions. Table I (End Matter) shows the number of cells and trajectories obtained under each experimental condition and the total number of cells (485 cells) and mobile trajectories (94,603 trajectories) used in the analysis. The five datasets exhibit considerable overlap, with slight deviations in the tail part of the PDFs. They can all be described by a stretched exponential distribution,

$$P_{on}(t_{on}) \propto e^{-(t_{on}/\tau_0)^{\beta}}. \tag{2}$$

The fitted values of the characteristic time τ_0 and the exponent β are reported in Table II (End Matter). The fitted values of β are found to vary from 0.61 to 0.78 (see Supplemental Material, Sec. III.B for details [38]).

To understand the origin of the stretched exponential distribution, we examine the effect of dynamic heterogeneity in individual trajectories, which vary significantly based on their values of p_{on} [see Fig. 1(c)]. Figure 2(b) shows the PDFs $P'_{on}(t_{on}/\langle t_{on}\rangle_i)$ of the normalized on-state dwell time $t_{on}/\langle t_{on}\rangle_i$. The PDFs $P'_{on}(t_{on}/\langle t_{on}\rangle_i)$ for different cell lines are found to follow the same exponential distribution over four decades of $t_{on}/\langle t_{on}\rangle_i$ once variations in $\langle t_{on}\rangle_i$ among different trajectories (dynamic heterogeneity) are divided out:

$$P'_{on}(t_{on}/\langle t_{on}\rangle_i) \propto e^{-a(t_{on}/\langle t_{on}\rangle_i)}. \tag{3}$$

(See End Matter and Supplemental Material, Sec. II.A for more results [38]).

The off-state dwell time t_{off} exhibits similar statistical properties as those of t_{on}. The PDFs $P_{off}(t_{off})$ for various vesicles across different cell types follow a stretched exponential distribution akin to Eq. (2) with $\beta = 0.30 \pm 0.04$ (see Fig. 3). A smaller value of β indicates a more stretched distribution, suggesting that t_{off} is subjected to greater heterogeneity. Furthermore, the PDFs $P'_{off}(t_{off}/\langle t_{off}\rangle_i)$ of the normalized dwell time $t_{off}/\langle t_{off}\rangle_i$ conform to the same exponential distribution (see Supplemental Material, Sec. II.B for more results [38]).

The exponential distributions of the PDFs $P'_{on}(t_{on}/\langle t_{on}\rangle_i)$ and $P'_{off}(t_{off}/\langle t_{off}\rangle_i)$ reveal common features of intracellular transport across different cell types and vesicles with various biochemical markers and functions (see Table II for more fitting results). These results suggest that transitions between the on and off states occur randomly over time, which can be modeled as a Poisson process with a transition rate $1/\langle t_{on}\rangle$

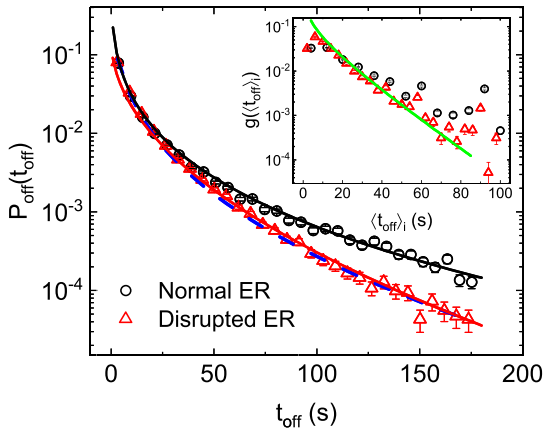

FIG. 3. Effects of ER disruption. Measured PDFs $P_{\rm off}(t_{\rm off})$ for EGFR endosomes in untreated BEAS-2B cells with a normal ER (black circles) and in treated cells with disrupted ER networks (red triangles). The black and red solid lines show the best fits to Eq. (2) with $\beta = 0.3 \pm 0.04$ ($\tau_0 = 0.11 \pm 0.08$ s) and $\beta = 0.5 \pm 0.03$ ($\tau_0 = 2.6 \pm 1$ s), respectively. The blue dashed line is the calculated $P_{\rm off}(t_{\rm off})$ using Eqs. (4) and (5) with $\beta = 0.5$ and $\tau_0 = 3.8$ s. The inset displays the measured $g(\langle t_{\rm off}\rangle_i)$ for untreated (black circles) and treated BEAS-2B cells (red triangles). The green solid line is a fit of Eq. (5) to red triangles with $\tau_0 = 3.6 \pm 0.1$ s. Slight variations in the fitted τ_0 result from fitting uncertainties in β.

[51]. When vesicles move along microtubules, they encounter many obstacles, which causes the transitions that are intrinsically stochastic. The on-state dwell time is primarily determined by unbinding events of motor proteins as they navigate the complex cytoskeletal network. The off-state dwell time, on the other hand, is the docking time for a motor-vesicle assembly finding a permissive path to move along.

The actual dwell time of individual vesicles in each state is influenced by the complex local environment in cytoplasm, where these transitions occur. As a result, the unconditional PDF $P(\tau)$ (with $\tau = t_{\rm on}$ or $t_{\rm off}$), which follows a stretched exponential distribution, may arise from a superposition of simple exponential distributions, originating from an ensemble of independent Poissonian binding and unbinding events of motor proteins, i.e.,

$$P(\tau) \propto e^{-(\tau/\tau_0)^\beta} = \int_0^\infty g(\tau_i) e^{-\tau/\tau_i} d\tau_i, \tag{4}$$

where $g(\tau_i)$ is a distribution function of the trajectory-based mean dwell time τ_i.

Figure 2(c) shows the distribution function $g(\langle t_{\rm on}\rangle_i)$ for different vesicles across various cell types. The five datasets exhibit considerable overlap, and the distribution of trajectory means $\langle t_{\rm on}\rangle_i$ is broad, spanning a range comparable to that of individual $t_{\rm on}$ values. Using the measured $g(\langle t_{\rm on}\rangle_i)$ for lysosomes in BEAS-2B cells, we calculate $P_{\rm on}(t_{\rm on})$ using the second equality in Eq. (4) [black dashed line in Fig. 2(a)], which shows a good agreement with the measured $P_{\rm on}(t_{\rm on})$. Equally good fittings are also obtained for other vesicle and cell types (see Fig. 4). Figure 2, thus, verifies the origin of stretched-exponential dwell time statistics, as shown in Eq. (4).

To further verify the above results obtained with normal cell types, we apply two separate cell treatments to alter the cytoskeletal conditions through which vesicular cargoes move across the cell (see Supplemental Material, Sec. I for experimental details [38]). One treatment significantly disrupts the morphology of the endoplasmic reticulum (ER) (see Supplemental Material, Fig. S10 and Sec. IV.A [38]). The ER is known to form an interconnected network with convoluted sheetlike and tubelike membrane structures that permeate the cytoplasm and was shown to establish pervasive, discrete physical contact with vesicles [52,53]. The other treatment alters cell volume, thereby altering intracellular crowdedness (see Supplemental Material Figs. S13 and S14 and Sec. IV.B [38]). These two cell treatments represent two essential biochemical and physical perturbations to the intracellular environment and are used to identify key factors contributing to the observed heterogeneity.

Because of reduced interactions with the disrupted ER network, the EGFR endosomes are drastically mobilized, with their immobile ratio decreased from 49% to 19% and their average $p_{\rm on}$ increased from 0.13 to 0.17. Figure 3 shows additional effects of disrupting the ER network. In the treated BEAS-2B cells, the PDF $P_{\rm off}(t_{\rm off})$ remains a stretched exponential form; however, the exponent β is increased from 0.3 to 0.5, indicating a reduced level of dynamic heterogeneity. The normalized PDF $P'_{\rm off}(t_{\rm off}/\langle t_{\rm off}\rangle_i)$ follows the same exponential distribution as that for untreated BEAS-2B cells (see Supplemental Material, Fig. S12 [38]).

The distribution function $g(\langle t_{\rm off}\rangle_i)$ also changes considerably (see inset of Fig. 3). The bulk region ($4s \le \langle t_{\rm off}\rangle_i \le 85$ s) of the obtained $g(\langle t_{\rm off}\rangle_i)$ can be well described by [31,32,54,55]

$$g(\tau_i) = \frac{1}{2\sqrt{\pi \tau_i \tau_0}} e^{-\tau_i/4\tau_0}, \tag{5}$$

where $\tau_i = \langle t_{\rm off}\rangle_i$ and $\tau_0 = 3.6 \pm 0.1$ s (green solid line). By substituting Eq. (5) into Eq. (4), one obtains an analytical form of the stretched exponential PDF with $\beta = 1/2$ (blue dashed line in Fig. 3), which agrees well with the experimental data. For other values of β (≤ 1), a series expansion presentation is available [32]. The bulk region of the obtained $g(\langle t_{\rm on}\rangle_i)$, where the experimental data are most reliable, can be well described by the series expansion, as shown in Fig. 2(c) (see Supplemental Material, Sec. III.C for details [38]). The off-state results shown in Fig. 3, as well as in Supplemental Material, Figs. S4–S8 [38], provide further support to the physical mechanism described in Eq. (4).

In contrast to the significant changes observed in the off state, the statistics of the on-state dwell time t_{on} remain largely unaffected by ER disruption (see Supplemental Material, Fig. S11 and Sec. IV.A [38]). As on-state EGFR endosomes move rapidly along microtubules, they have limited time to interact with the ER network, thereby reducing the impact of ER disruption. By contrast, off-state EGFR endosomes exhibit slower movement and greater resistance due to prolonged interactions with the ER network and other obstacles, which explains the significant impact of ER disruption on $P_{off}(t_{off})$.

Our results, thus, provide new insights into the intricate interplay between motor-driven endosomal transport and various resistive forces arising from interactions with cytoskeleton. First, we find that on-state vesicles inhabit a local environment that is significantly different, in terms of dynamic heterogeneity, from that in the off state. The measured $g(\langle t_{on}\rangle_i)$ covers a narrower range of $\langle t_{on}\rangle_i$, giving rise to a larger β closer to unity. The shape of the measured $g(\langle t_{on}\rangle_i)$ remains largely unchanged across various vesicle and cell types [see Fig. 2(c)]. This stability suggests that the local environment surrounding the microtubules facilitates a smoother pathway for motor-driven cargo transport with a high efficiency.

Second, when vesicles encounter strong pinning forces, such as physical tethering to the ER network [52,53], obstructions caused by actin patches or microtubule intersections [23,24,56], or opposing forces exerted by different types of motor proteins acting on the same vesicle [57,58], they enter the off state. In this case, the measured $g(\langle t_{off}\rangle_i)$ exhibits a broader range of $\langle t_{off}\rangle_i$, resulting in a smaller value of β. Furthermore, the shape of $g(\langle t_{off}\rangle_i)$ becomes sensitive to vesicle types and cell lines involved (see inset of Fig. 3 and Supplemental Material, Fig. S4(c) [38]). This result suggests that variations in the off-state value of β provide a more effective measure of their biological specificity (see Table II and Supplemental Material, Sec. IV.A [38]).

The dependence of cargo transport on interactions with the local environment is further illustrated by the effects of ER network disruption, which reduces dynamic heterogeneity, and by reinforcing such interactions, for example, through increased cytoplasmic crowding (see Supplemental Material, Sec. IV.B for details [38]). These results underscore the critical role of the intracellular context in regulating cargo transport dynamics in both on and off states, thereby promoting efficient cargo delivery in cells.

Intracellular cargo transport is a complex, multifaceted process that involves motor-vesicle assemblies, their viscoelastic interactions with the surrounding cytosol and cytoskeleton, and specific binding interactions with microtubules. A previous study [26] reported that the PDF $\mathcal{P}(\ell)$ of the directional persistence length ℓ exhibits a power-law tail and attributed this behavior to truncated Lévy walks. However, because ℓ is a composite variable that depends on the on-state velocity v, the dwell times t_{on} and t_{off}, and the effective diffusivity D during the off state, the physical interpretation of the conditional PDF $\mathcal{P}(\ell)$ is rather convoluted. In contrast, our analysis focuses on the dwell time in the on and off states, a simple and foundational variable in the two-state motion of motor-driven vesicles, thereby providing a clearer physical picture of intracellular cargo transport.

Acknowledgments—This work was supported by RGC and ITC of Hong Kong SAR under Grants No. 16300224 (P. T.), No. 16302025 (P. T.), No. C6041-24G (P. T.), No. 16104223 (P. H.), and No. ITCPD/17-9 (P. H.), and by NSTC of Taiwan under Grant No. 115-2112-M008-014-MY3 (P.-Y. L.).

Data availability—There are no publicly available research data or software supporting this manuscript. Requests for further information or data should be sent to the authors.

[1] F. Höfling and T. Franosch, Anomalous transport in the crowded world of biological cells, Rep. Prog. Phys. **76**, 046602 (2013).
[2] A. Triller and D. Choquet, New concepts in synaptic biology derived from single-molecule imaging, Neuron **59**, 359 (2008).
[3] D. A. Rusakov, L. P. Savtchenko, K. Zheng, and J. M. Henley, Shaping the synaptic signal: Molecular mobility inside and outside the cleft, Trends Neurosci. **34**, 359 (2011).
[4] C. P. Brangwynne, G. H. Koenderink, F. C. MacKintosh, and D. A. Weitz, Intracellular transport by active diffusion, Trends Cell Biol. **19**, 423 (2009).
[5] K. Jacobson, P. Liu, and B. C. Lagerholm, The lateral organization and mobility of plasma membrane components, Cell **177**, 806 (2019).
[6] S. Stam and M. L. Gardel, Cutting through the noise: The mechanics of intracellular Transport, Dev. Cell **30**, 365 (2014).
[7] S. S. Mogre, A. I. Brown, and E. F. Koslover, Getting around the cell: Physical transport in the intracellular world, Phys. Biol. **17**, 061003 (2020).
[8] A. Kusumi, Y. Umemura, N. Morone, and T. Fujiwara, in *Anomalous Transport: Foundations and Applications*, edited by R. Klages, G. Radons, and I. M. Sokolov (Wiley-VCH, Weinheim, 2008), Chap. 19, pp. 545–574.
[9] K. Ritchie, X.-Y. Shan, J. Kondo, K. Iwasawa, T. Fujiwara, and A. Kusumi, Detection of non-Brownian diffusion in the cell membrane in single molecule tracking, Biophys. J. **88**, 2266 (2005).
[10] A. V. Weigel, B. Simon, M. M. Tamkun, and D. Krapfa, Ergodic and nonergodic processes coexist in the plasma membrane as observed by single-molecule tracking, Proc. Natl Acad. Sci. U.S.A. **108**, 6438 (2011).
[11] W. He, H. Song, Y. Su, L. Geng, B. J. Ackerson, H. B. Peng, and P. Tong, Dynamic heterogeneity and non-Gaussian statistics for acetylcholine receptors on live cell membrane, Nat. Commun. **7**, 11701 (2016).
[12] W. He, Y. Su, H. B. Peng, and P. Tong, Dynamic heterogeneity and non-Gaussian statistics for ganglioside GM1s and acetylcholine receptors on live cell membrane, Mol. Biol. Cell **31**, 1380 (2020).

[13] B. Wang, S. M. Anthony, S. C. Baea, and S. Granick, Anomalous yet Brownian, Proc. Natl Acad. Sci. U.S.A. **106**, 15160 (2009).
[14] W. Chen and K. To, Unusual diffusion in a quasi-two-dimensional granular gas, Phys. Rev. E **80**, 061305 (2009).
[15] C. Xue, X. Zheng, K. Chen, Y. Tian, and G. Hu, Probing non-Gaussianity in confined diffusion of nanoparticles, J. Phys. Chem. Lett. **7**, 514 (2016).
[16] A. V. Chechkin, F. Seno, R. Metzler, and I. M. Sokolov, Brownian yet non-Gaussian diffusion: From superstatistics to subordination of diffusing diffusivities, Phys. Rev. X **7**, 021002 (2017).
[17] M. J. Saxton, A biological interpretation of transient anomalous subdiffusion. I. Qualitative model, Biophys. J. **92**, 1178 (2007).
[18] R. Metzlera, Superstatistics and non-Gaussian diffusion, Eur. Phys. J. Special Topics **229**, 711728 (2020).
[19] C. Beck and E. G. D. Cohen, Superstatistics, Physica A (Amsterdam) **322**, 267 (2003).
[20] M. V. Chubynsky and G. W. Slater, Diffusing diffusivity: A model for anomalous, yet Brownian, diffusion, Phys. Rev. Lett. **113**, 098302 (2014).
[21] B. Wang, J. Kuo, S. C. Bae, and S. Granick, When Brownian diffusion is not Gaussian, Nat. Mater. **11**, 481 (2012).
[22] T. A. Waigh and N. Korabel, Heterogeneous anomalous transport in cellular and molecular biology, Rep. Prog. Phys. **86**, 126601 (2023).
[23] A. L. Zajac, Y. E. Goldman, E. L. F. Holzbaur, and E. M. Ostap, Local cytoskeletal and organelle interactions impact molecular-motor-driven early endosomal trafficking, Curr. Biol. **23**, 1173 (2013).
[24] Ŭ. Bálint, I. Verdeny Vilanova, Á. Sandoval Álvarez, and M. Lakadamyali, Correlative live-cell and superresolution microscopy reveals cargo transport dynamics at microtubule intersections, Proc. Natl Acad. Sci. U.S.A. **110**, 3375 (2013).
[25] D. Arcizet, B. Meier, E. Sackmann, J. O. Rädler, and D. Heinrich, Temporal analysis of active and passive transport in living cells, Phys. Rev. Lett. **101**, 248103 (2008).
[26] K. Chen, B. Wang, and S. Granick, Memoryless self-reinforcing directionality in endosomal active transport within living cells, Nat. Mater. **14**, 589 (2015).
[27] A. I. D'Souza, R. Grover, G. A. Monzon, L. Santen, and S. Diez, Vesicles driven by dynein and kinesin exhibit directional reversals without regulators, Nat. Commun. **14**, 7532 (2023).
[28] A. Serra-Marques *et al.*, Concerted action of kinesins KIF5B and KIF13B promotes efficient secretory vesicle transport to microtubule plus ends, eLife **9**, e61302 (2020).
[29] J. C. Phillips, Stretched exponential relaxation in molecular and electronic glasses, Rep. Prog. Phys. **59**, 1133 (1996).
[30] R. Richert and M. Richert, Dynamic heterogeneity, spatially distributed stretched-exponential patterns, and transient dispersions in solvation dynamics, Phys. Rev. E **58**, 779 (1998).
[31] P. Y. Lai, Relaxation time spectrum in glassy states, Chin J. Phys. **33**, 271 (1995).
[32] D. C. Johnston, Stretched exponential relaxation arising from a continuous sum of exponential decays, Phys. Rev. B **74**, 184430 (2006).
[33] G. Williams and D. C. Watts, Non-symmetrical dielectric relaxation behavior arising from a simple empirical decay function, Trans. Faraday Soc. **66**, 80 (1970).
[34] C. P. Lindsey and G. D. Patterson, Detailed comparison of the Williams–Watts and Cole–Davidson functions, J. Chem. Phys. **73**, 3348 (1980).
[35] Y.-S. Shen, C.-J. Luo, Y. Wen, W. He, P. Huang, H.-Y. Chen, P.-Y. Lai, and P. Tong, Directed motion of membrane proteins under an entropy-driven potential field generated by anchored proteins, Phys. Rev. Res. **3**, 043195 (2021).
[36] J. S. Bonifacino and J. Neefjes, Moving and positioning the endolysosomal system, Curr. Opin. Cell Biol. **47**, 1 (2017).
[37] J. Bakker, M. Spits, J. Neefjes, and I. Berlin, The EGFR odyssey–from activation to destruction in space and time, J. Cell Sci. **130**, 4087 (2017).
[38] See Supplemental Materials at http://link.aps.org/supplemental/10.1103/ngxy-z1d3 for further details, which includes Refs. [39–49].
[39] J. Krebs, L. B. Agellon, and M. Michalak, Ca^{2+} homeostasis and endoplasmic reticulum (ER) stress: An integrated view of calcium signaling, Biochem. Biophys. Res. Commun. **460**, 114 (2015).
[40] Y. Shen, D. Guan, D. Serien, S. Takeuchi, P. Tong, L. Yobas, and P. Huang, Mechanical characterization of microengineered epithelial cysts by using atomic force microscopy, Biophys. J. **112**, 398 (2017).
[41] Y. Shen and K. M. Ori-McKenney, Microtubule-associated protein MAP7 promotes tubulin posttranslational modifications and cargo transport to enable osmotic adaptation, Dev. Cell **59**, 1553 (2024).
[42] J. C. Crocker and D. G. Grier, Methods of digital video microscopy for colloidal studies, J. Colloid Interface Sci. **179**, 298 (1996).
[43] S. Anthony, L. Zhang, and S. Granick, Methods to track single-molecule trajectories, Langmuir **22**, 5266 (2006).
[44] A. M. Law, *Simulation Modeling and Analysis*, 5th ed. (McGraw-Hill Education, New York, 2015), pp. 335–344.
[45] J. P. Nolan, Fitting data and assessing goodness-of-fit with stable distributions, in *Applications of Heavy Tailed Distributions in Economics, Engineering and Statistics* (American University, Washington, DC, 1999).
[46] Y. Shibata, G. K. Voeltz, and T. A. Rapoport, Rough sheets and smooth tubules, Cell **126**, 435 (2006).
[47] J. Nixon-Abell *et al.*, Increased spatiotemporal resolution reveals highly dynamic dense tubular matrices in the peripheral ER, Science **354**, aaf3928 (2016).
[48] H. Wu, P. Carvalho, and G. K. Voeltz, Here, there, and everywhere: The importance of ER membrane contact sites, Science **361**, eaan5835 (2018).
[49] H. Li, S. X. Dou, Y. R. Liu, W. Li, P. Xie, W. C. Wang, and P. Y. Wang, Mapping intracellular diffusion distribution using single quantum dot tracking: compartmentalized diffusion defined by endoplasmic reticulum, J. Am. Chem. Soc. **137**, 436 (2015).
[50] M. Röding, M. Guo, D. A. Weitz, M. Rudemo, and A. Särkkä, Identifying directional persistence in intracellular particle motion using hidden Markov models, Math. Biosci. **248**, 140 (2014).
[51] P. Hänggi, P. Talkner, and M. Borkovec, Reaction-rate theory: Fifty years after Kramers, Rev. Mod. Phys. **62**, 251 (1990).
[52] M. L. M. Jongsma *et al.*, An ER-associated pathway defines endosomal architecture for controlled cargo transport, Cell **166**, 152 (2016).

[53] M. J. Phillips and G. K. Voeltz, Structure and function of ER membrane contact sites with other organelles, Nat. Rev. Mol. Cell Biol. **17**, 69 (2016).
[54] C. P. Lindsey and G. D. Patterson, Detailed comparison of the Williams–Watts and Cole–Davidson functions, J. Chem. Phys. **73**, 3348 (1980).
[55] E. Helfand, On inversion of the Williams–Watts function for large relaxation times, J. Chem. Phys. **78**, 1931 (1983).
[56] B. van Bommel, A. Konietzny, O. Kobler, J. Bär, and M. Mikhaylova, F-actin patches associated with glutamatergic synapses control positioning of dendritic lysosomes, EMBO J. **38**, e101183 (2019).
[57] W. O. Hancock, Bidirectional cargo transport: Moving beyond tug of war, Nat. Rev. Mol. Cell Biol. **15**, 615 (2014).
[58] A. G. Hendricks, E. Perlson, J. L. Ross, H. W. Schroeder III, M. Tokito, and E. L. Holzbaur, Motor coordination via a tug-of-war mechanism drives bidirectional vesicle transport, Curr. Biol. **20**, 697 (2010).

End Matter

Summary of sample sizes—Details about the sample sizes used in this Letter are summarized in Table I. To build up the statistics, we typically track each type of vesicles from more than 39 cells cultured under the same condition so that at least 4.7×10^3 trajectories were used for statistical analysis.

Summary of fitting results—The fitting results for on-state dwell time t_{on} and off-state dwell time t_{off} are summarized in Table II.

Statistical properties of on-state dwell time t_{on}—Figure 4 shows the individual plot of the PDFs $P_{on}(t_{on})$ in Fig. 2(a), along with the fits for each dataset. It is seen that the level of agreement between the experimental results and the stretched-exponential fit [Eq. (2)], as well as the calculated $P_{on}(t_{on})$ using Eq. (4), remains equally good for each dataset.

Statistical properties of normalized on-state dwell time $t_{on}/\langle t_{on}\rangle_i$—Figure 5 shows the individual plot of the PDFs $P'_{on}(t_{on}/\langle t_{on}\rangle_i)$ in Fig. 2(b), along with the fits for each dataset. It is seen that the level of agreement between the experimental results and the exponential fit [Eq. (3)], remains equally good for each dataset.

TABLE I. Summary of cell treatments and sample sizes. The columns, from left to right, provide information on the cell types used, the types of vesicles imaged, the treatments applied to the cells, the number of cells that were imaged, and the total number of mobile trajectories included in the statistical analysis.

Cell type	Vesicle type	Cell treatment	No. of cells	No. of mobile trajectories
BEAS-2B	EGFR endosome	No treatment	83	9946
BEAS-2B	EGFR endosome	ER disruption	66	9673
BEAS-2B	Early endosome	No treatment	39	20,780
BEAS-2B	Lysosome	No treatment	42	17,465
BEAS-2B	EGFR endosome	Hypotonic	63	9217
BEAS-2B	EGFR endosome	Isotonic	49	8846
BEAS-2B	EGFR endosome	Hypertonic	48	4752
HeLa	EGFR endosome	No treatment	51	6007
RPE-1	EGFR endosome	No treatment	44	7917
Total:			485	94,603

TABLE II. Summary of fitting results. The first two rows present the best-fit values of the parameters β and τ_0 for the stretched exponential distribution in Eq. (2) and Supplemental Material, Eq. (S1), applied to the measured PDFs from various vesicle types, cell lines, and cell treatments. The last two rows provide the best-fit values of the parameter a for the exponential distribution in Eq. (3) and Supplemental Material, Eq. (S2), applied to the measured PDFs from various vesicle types, cell lines, and cell treatments. Error bars indicate the fitting uncertainties.

	EGFR endosome BEAS-2B	Lysosome BEAS-2B	Early endosome BEAS-2B	EGFR endosome HeLa	EGFR endosome RPE-1	EGFR endosome BEAS-2B ER disruption	BEAS-2B EGFR endosome hypotonic	BEAS-2B EGFR endosome isotonic	BEAS-2B EGFR endosome hypertonic
t_{on} β	0.78 ± 0.05	0.72 ± 0.04	0.72 ± 0.03	0.70 ± 0.03	0.61 ± 0.04	0.70 ± 0.05	0.75 ± 0.05	0.64 ± 0.04	0.57 ± 0.04
t_{on} τ_0 (s)	0.84 ± 0.10	0.56 ± 0.10	0.54 ± 0.10	0.49 ± 0.10	0.29 ± 0.10	0.56 ± 0.10	0.70 ± 0.10	0.38 ± 0.10	0.23 ± 0.07
t_{off} β	0.30 ± 0.04	0.46 ± 0.04	0.39 ± 0.03	0.42 ± 0.04	0.36 ± 0.03	0.50 ± 0.03	0.48 ± 0.04	0.38 ± 0.04	0.32 ± 0.04
t_{off} τ_0 (s)	0.11 ± 0.08	1.70 ± 0.70	0.65 ± 0.30	1.11 ± 0.50	0.48 ± 0.20	2.60 ± 1.00	2.00 ± 0.80	0.54 ± 0.30	0.26 ± 0.20
$t_{on}/\langle t_{on}\rangle_i$ a	1.60 ± 0.04	1.70 ± 0.05	1.60 ± 0.05	1.68 ± 0.06	1.55 ± 0.05	1.58 ± 0.05	1.62 ± 0.07	1.59 ± 0.06	1.61 ± 0.06
$t_{off}/\langle t_{off}\rangle_i$ a	0.99 ± 0.04	1.25 ± 0.05	1.10 ± 0.05	0.97 ± 0.06	1.02 ± 0.06	1.03 ± 0.05	1.11 ± 0.07	1.00 ± 0.07	1.00 ± 0.07

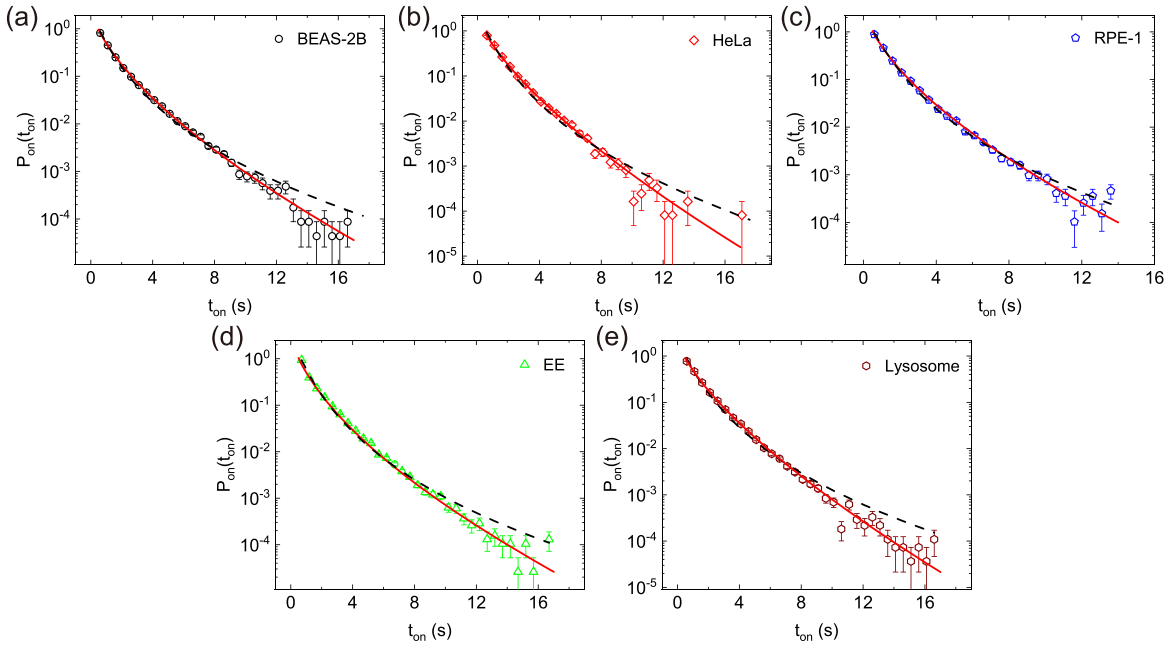

FIG. 4. Statistics of on-state dwell time t_{on}. Individual plot of the measured PDFs $P_{on}(t_{on})$ in Fig. 2(a): EGFR endosomes in (a) BEAS-2B, (b) HeLa, and (c) RPE-1 cells; (d) early endosomes (EE) and (e) lysosomes in BEAS-2B cells. The red solid lines show the stretched exponential fits [Eq. (2)] to each dataset. The black dashed lines show the calculated $P_{on}(t_{on})$ using Eq. (4) for each dataset. The fitting parameters for all the datasets are reported in Table II.

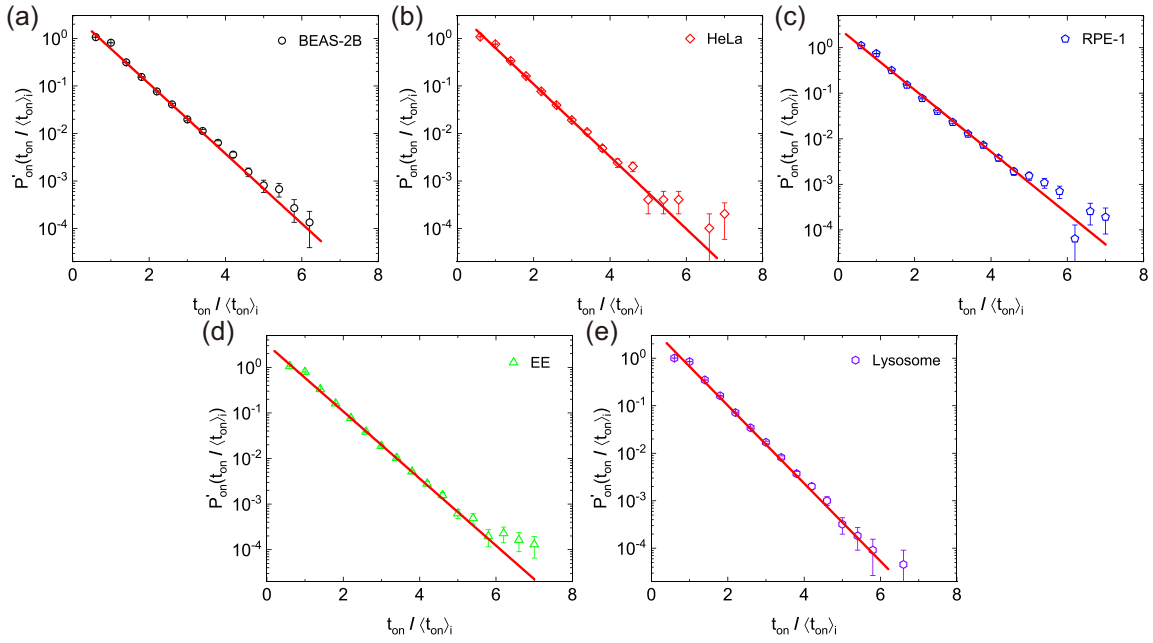

FIG. 5. Statistics of normalized on-state dwell time $t_{on}/\langle t_{on}\rangle_i$. Individual plot of the measured PDFs $P'_{on}(t_{on}/\langle t_{on}\rangle_i)$ in Fig. 2(b): EGFR endosomes in (a) BEAS-2B, (b) HeLa, and (c) RPE-1 cells; (d) early endosomes (EE) and (e) lysosomes in BEAS-2B cells. The red solid lines show the exponential fits [Eq. (3)] to each dataset. The fitting parameters for all the datasets are reported in Table II.